THE JOURNAL OF PHYSICAL CHEMISTRY C
A JOURNAL OF THE AMERICAN CHEMICAL SOCIETY

pubs.acs.org/JPCC
Article

A Comprehensive Overview of Active Sites of fcc-Co Nanoparticles and Their Role in CO Splitting—A DFT Study

Enrico Sireci, Dmitry I. Sharapa, and Felix Studt*

Cite This: J. Phys. Chem. C 2025, 129, 21634−21641
Read Online

ACCESS | Metrics & More | Article Recommendations | Supporting Information

ABSTRACT: When modeling catalytically active sites in fcc metal nanoparticles (NPs), most theoretical studies often rely on just a handful of low-index surfaces, which might lead to overlooking surface sites that are important in the reaction. In this work, we identify 13 distinct types of low-coordinated sites (LCS) on fcc-Co catalysts and keep track of their concentration evolution with particle size. By calculating CO dissociation barriers, we show that these sites are characterized by significantly different reactivities and discover active sites with lower barriers than previously known. In addition, we classify the most active sites of small Co nanoparticles that are typically not modeled. More generally, this work provides guidance in choosing relevant surface models based on particle sizes.

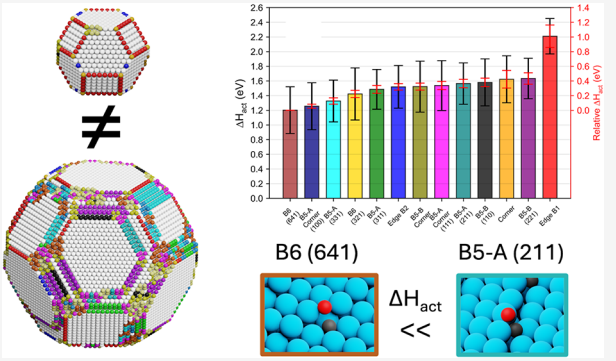

1. INTRODUCTION

Supported transition metal (TM) nanoparticles (NPs) are the catalysts of choice for a large number of chemical processes, including ammonia synthesis,[1−3] methanol synthesis,[4−6] and the Fischer−Tropsch (FT) reaction.[7−9] The specifics of the reaction mechanisms on these catalysts are ranging from comprehensively understood (e.g., ammonia synthesis)[10−12] to vividly debated (FT).[13−16] To this account, calculations of surface processes using density functional theory (DFT) as a tool toward a deeper understanding of rate-limiting steps have gained traction in the past decades, owing to the progress that has been achieved both in terms of accuracy but also computational speed.[17−19]

However, the main limitations of DFT seem to be the choice of catalyst model, i.e., the surface (or active site motif) that is chosen as it is believed to be the most representative of the employed supported NP. For fcc metals, the close-packed (111) and (100) surfaces are among the most typical choices, as they are the simplest and most common surface sites but also due to the plethora of highly sophisticated surface science experiments carried out on these facets, providing the urgently needed benchmark for DFT.[20−29] Many heterogeneous reactions exhibit a high surface sensitivity, especially when strong double or triple bonds are to be activated or broken.[30] This is often explained in light of the increase in concentration of under-coordinated step and kink sites (i.e., B5 and B6 sites) with increasing particle size for crystals smaller than ∼10−15 nm.[10,31−34] For example, B5 and B6 sites have been suggested to be the active sites for C−O bond breaking for the Co-based FT reaction.[15,16,32,35−39] Interestingly, while the number of low-coordinated atoms on NP surfaces increases with decreasing particle size (both when normalized to surface area and number of atoms),[40−43] not all of these sites are thought to be highly active for N−N and C−O bond breaking reactions, although this has hardly been explored theoretically to date.[44] Often, undercoordinated sites on smaller particles are modeled as steps and kinks of larger extended surfaces, e.g., fcc(211), fcc(321) etc., and the results of this modeling are used to explain their activity or lack thereof.[35−37,45−55] Herein, we perform a comprehensive study comparing the activity of all plausible surface sites of small and large fcc NPs by means of DFT using the dissociation of CO on fcc-Co surfaces as a probe reaction. We show that there are sites showcasing high activity that have so far been neglected and also highlight that the commonly used step sites thought to represent small NPs for the most part fail to describe the reality.

2. METHODS

Spin-polarized DFT calculations were performed with the software VASP version 6.2[56,57] employing the GGA functional BEEF-vdW[58] and using the projector-augmented wave (PAW) method with standard PAW potentials.[59] Gaussian smearing with a width of 0.1 eV was used in all calculations, and the sampling of the Brillouin zone was carried out in a Monkhorst−

Received: October 23, 2025
Revised: November 10, 2025
Accepted: November 11, 2025
Published: November 24, 2025

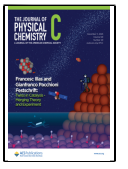

https://doi.org/10.1021/acs.jpcc.5c07278
J. Phys. Chem. C 2025, 129, 21634−21641

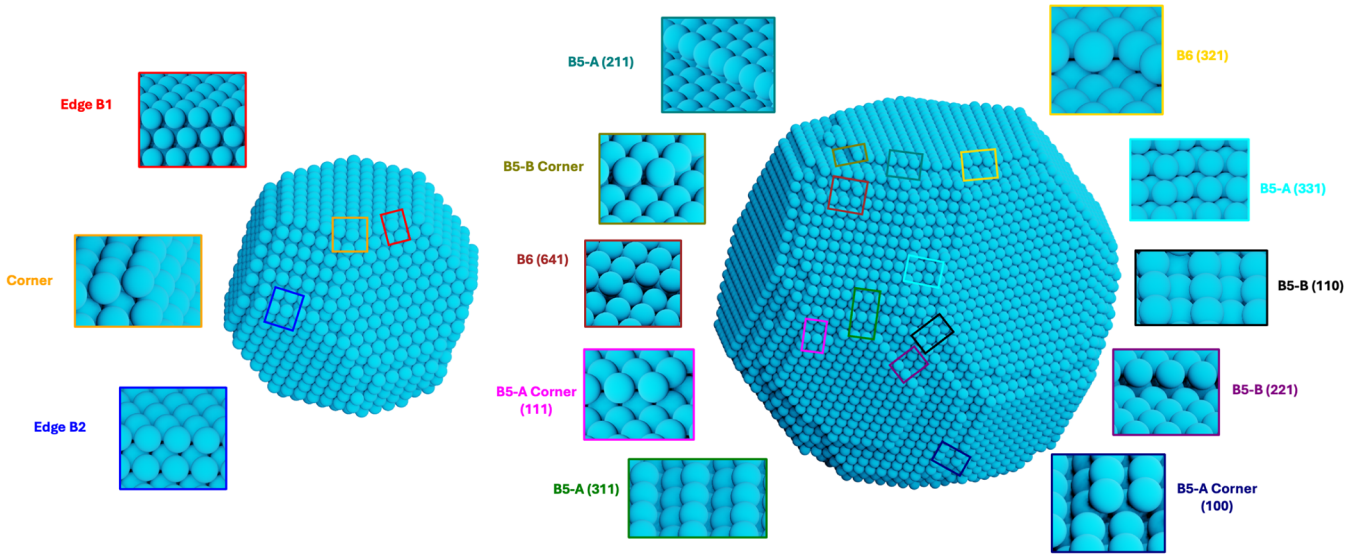

Figure 1. Different sites identified in this study are highlighted on 4 (left) and 8 (right) nm Co NPs using data published elsewhere.[33]

Pack grid with a *k*-point density of approximately 36 *k*-points per $Å^{-1}$, that is

a $(3 \times 5 \times 1)$ grid for the $(1 \times 3 \times 4)$ Edge B1, $(2 \times 3 \times 4)$ fcc-Co(311), $(2 \times 3 \times 4)$ fcc-Co(211), $(2 \times 3 \times 4)$ fcc-Co(331), and $(3 \times 3 \times 4)$ fcc-Co(110) cells;
a $(5 \times 5 \times 1)$ grid for the $(1 \times 3 \times 4)$ Edge B2 cell;
a $(5 \times 2 \times 1)$ grid for the $(3 \times 2 \times 4)$ fcc-Co(221) cell;
a $(3 \times 2 \times 1)$ grid for the $(2 \times 2 \times 4)$ fcc-Co(321), $(1 \times 1 \times 4)$ B5 Corner (111), and B5 Corner (100) cells;
a $(3 \times 3 \times 1)$ grid for the $(2 \times 2 \times 4)$ fcc-Co(641), and the $(1 \times 1 \times 4)$ Corner cells.

Snapshots of the top and side views of all the unit cells (highlighting the frozen Co atoms) along with their *x*, *y*, and *z* dimensions and *k*-point grids are given in Figures S1−S12. Bulk calculation for fcc-Co was carried out with an energy cutoff of 600 eV, which was changed to 400 eV for all the other calculations. Convergence of the SCF cycle was set at an energy difference of 10^{-6} eV, while ionic convergence was achieved when the atomic forces were below 0.01 eV/Å. The transition state search was carried out using the improved dimer method as implemented in VASP,[60] for which we used the same energy and force convergence thresholds as for the other geometry optimizations. In all calculations, we considered four-layer slab models, where the bottom two layers were frozen in the bulk fcc-Co configuration. All the calculations are carried out in the low coverage regime, being 1/5 for the fcc-Co(641) surface, 1/4 for the fcc-Co(321) and corner surfaces, and 1/3 for all the others when only step atoms are considered. We note that the definition of coverage is rather arbitrary for some surfaces such as the ones where corners are modeled. We made sure that the coverage of CO when normalized to all surface atoms is small (always below 1/12 of a CO molecule per surface Co atom) and that adsorbed CO molecules are always separated by at least 7.5 Å, except for Edge B2 where the CO images are 7.1 Å apart. Gunasooriya et al. reported a small CO adsorption energy change of 5 kJ/mol when increasing the coverage from 1/9 to 1/3 ML (i.e., reducing the distance between the periodic images of CO molecules from ∼7.5 to ∼4.3 Å) on the *hcp*(0001) surface.[61] This highlights that the effect of lateral interactions for CO on Co typically comes into play for coverages higher than the ones considered in this study. Furthermore, it has been previously reported that the calculation of direct CO dissociation barriers on corrugated Co surfaces is nearly independent of surface coverage.[62] All models had at least 15 Å of vacuum in the *z*-direction. All of the reaction pathways are corrected for zero-point energy (ZPE) contributions. Vibrational analysis to estimate ZPEs was carried out with the finite differences method with atomic displacements of 0.02 Å and only include the adsorbed CO. All transition states were confirmed through a vibrational analysis that yielded only one imaginary frequency located along the reaction path. The *xyz* coordinates of all the structures and their respective energies are provided in the SI. All the NP models discussed in this study are taken from our recent work,[33] where further details about the employed Monte Carlo algorithm are provided. In short, we employ a lattice model in which Co atoms are redistributed in a fixed fcc grid, and their energy is estimated based on their nearest-neighbor coordination number (CN) using unsupported fcc-Co NP structures of particle sizes 2, 4, 6, 8, and 10 nm corresponding to 376, 3008, 10,152, 24,064, and 47,000 atoms, respectively. The site identification scheme is based on the classification of the empty sites in the fcc grid that are adjacent to grid positions occupied by Co atoms. Thus, depending on the number of neighboring occupied sites, we define B1, B2, 2B3, B4, B5, and B6 sites according to the scheme proposed by van Hardeveld and Hartog.[63] The different types of B*x* sites are further distinguished based on criteria concerning the CN of the neighboring Co atoms and of the next-neighboring Co atoms that are presented in Section S2.

3. RESULTS AND DISCUSSION

Our starting point is recently developed paired DFT-Monte Carlo (MC) simulations that are able to produce models of fcc-Co NPs as a function of temperature, particle size, and metal−support interactions (MSI).[33] Importantly, this method yields a realistic picture of the shape of metal NPs including the presence of irregularities and defects on the surface. Figure 1 illustrates simulated Co particles with the sizes of 4 nm (left) and 8 nm (right), where the various low coordinated sites (LCS) occurring on their surfaces are highlighted. On the 4 nm NP, corner sites and the two types of edge sites (Edge B1 and Edge B2, located at the (111)/(111) and (111)/(100) intersections,

https://doi.org/10.1021/acs.jpcc.5c07278
J. Phys. Chem. C 2025, 129, 21634−21641

respectively) are mostly present, while the 8 nm NP has a plethora of unique surface sites. We highlight five different B5-A, three B5-B, and two B6 sites. B5-A sites are steps located at the intersections between (111) and (100) terraces. When they are found in two or more consecutive step rows, they are classified as B5-A (311). When this is not the case, they can either be located on a (111) or a (100) terrace and are classified as B5-A (211) sites and B5-A (331) sites, respectively. B5-A sites adjacent to corners were additionally denoted as B5-A Corner (111) or B5-A Corner (100) depending on whether they are located on a (111) or (100) terrace. B5-B step sites are found at the intersections between two (111) terraces. Similarly to B5-A sites, when they are found in two or more consecutive step rows, they are classified as B5-B (110), while when they are found on a terrace, they are called B5-B (221). B5-B sites next to a corner are classified as B5-B corner sites. Lastly, the two identified types of B6 kink sites are the B6 (321) and B6 (641) when they are found on a (111) and (100) terrace, respectively. Further details about site identification are given in Section S2

As evident from Figure 1, the nature and occurrence of these various surface sites change drastically with size. This change is quantified in Figure 2a, where the relative percentages of each site as a function of the particle size are presented. In particular, we witness a gradual substitution, symmetric around D_{Co} = 6 nm, of the edges and corners with steps and kinks. Corners are largely present on the 2 nm NPs, accounting for slightly less than 40% of the total LCS, but their concentration decreases fast with particle size, as already from D_{Co} = 6 nm they account for less than 5%. Edge sites, for which the B2 type, except for the smallest particles, prevails over the B1, are the predominant LCS up to 4 nm, where they reach their maximum of 64%, and decrease fast afterward, accounting for roughly 10% of the total LCS in the 10 nm NPs. B5-A and B5-B sites are always present in similar proportions, even though the former grows somewhat faster with increasing D_{Co}. Taken together, these sites become the predominant LCS from D_{Co} = 6 nm. B6 sites are mostly absent in the smallest particles but increase steadily with D_{Co} and peak at ∼17% of the total LCS for the 10 nm NP. The B6 (321) sites appear from D_{Co} = 6 nm but grow faster than the (641) type, resulting in the two B6 sites being present in equal proportions for D_{Co} = 10 nm. In summary, while in the 2−4 nm size range LCS are best described by corners and edges, in the 8−10 nm range step and kink sites become more common. Particles of about 6 nm are the most diverse, since all sites except corners are present in notable proportions. In Figure 2b, we present the percentage of the different LCS normalized to the total number of surface sites (i.e., with the inclusion of 2B3 and B4 terrace sites), which reveals that the initial decrease of edges and corners is later compensated by the increase of B5 and B6 sites, which causes a minimum in the surface concentration of LCS for D_{Co} = 6 nm. This also explains the reported trend for the number of LCS normalized to the number of Co atoms shown in Figure 2c, characterized by an initial fast decrease of the cumulative number of LCS with particle size that stays roughly constant for D_{Co} > 6 nm, despite the further decrease of the surface/volume ratio of the NPs.

Interestingly, the local geometries of the edges and corners on the small particles (which we call here Edge B1, Edge B2, and Corner sites) are distinctly different from the undercoordinated sites on the larger particles (e.g., all B5 and B6 sites) in that they do not provide pockets where dissociated atoms can adsorb strongly. Nevertheless, B5 sites, such as (211) step edges, are often cited as prototypical low-coordinated sites that are

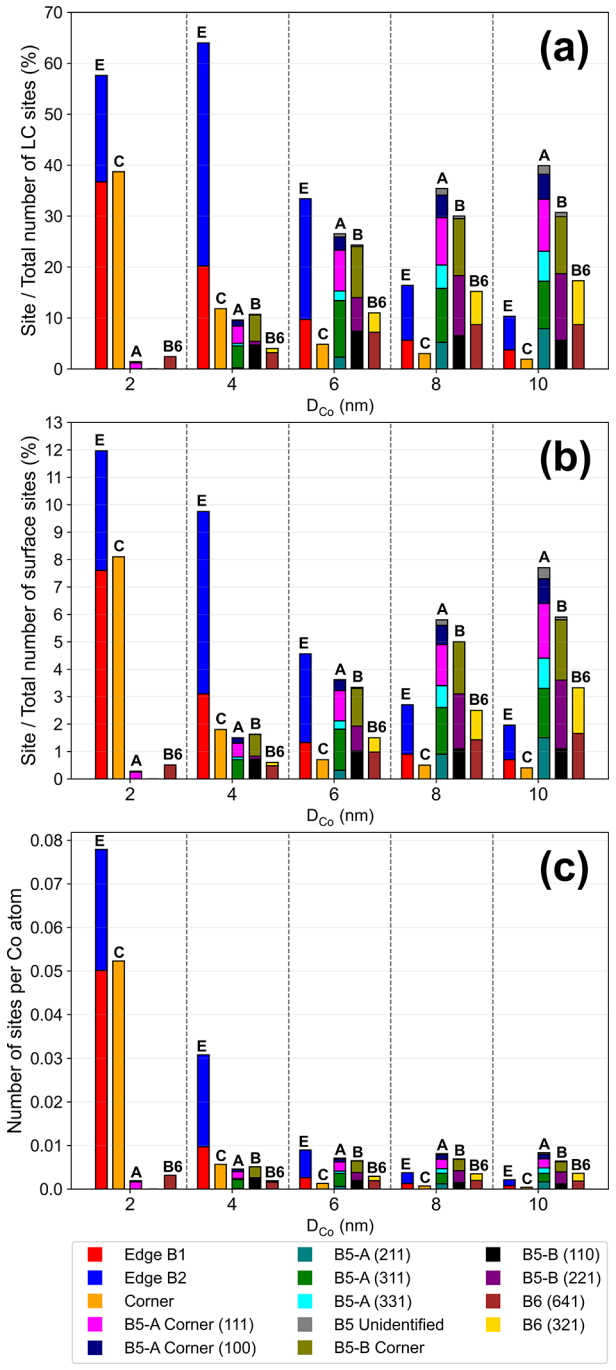

Figure 2. Percentages of each of the considered sites with respect to (a) the total number of low-coordinated sites and (b) the total number of surface sites and (c) number of sites per number of Co atoms of unsupported Co NP as a function of increasing particle diameter (D_{Co}), with data taken from previously published work.[33]

presumably more abundant on smaller particles.[64−69] We were therefore interested in how these sites perform compared to the Edge B1, Edge B2, and Corner sites. We investigated this by calculating CO dissociation pathways on all possible surfaces depicted in Figure 1, the results of which are shown in Figure 3. In this reaction framework, CO first adsorbs on a top position, migrates to the base of the site, and then splits into C* and O*. As shown in Figures S15−S26, with the exception of the B6 (641) and B5 Corner (111) sites, CO always adsorbs preferentially on top sites, in agreement with experimental

https://doi.org/10.1021/acs.jpcc.5c07278
J. Phys. Chem. C 2025, 129, 21634−21641

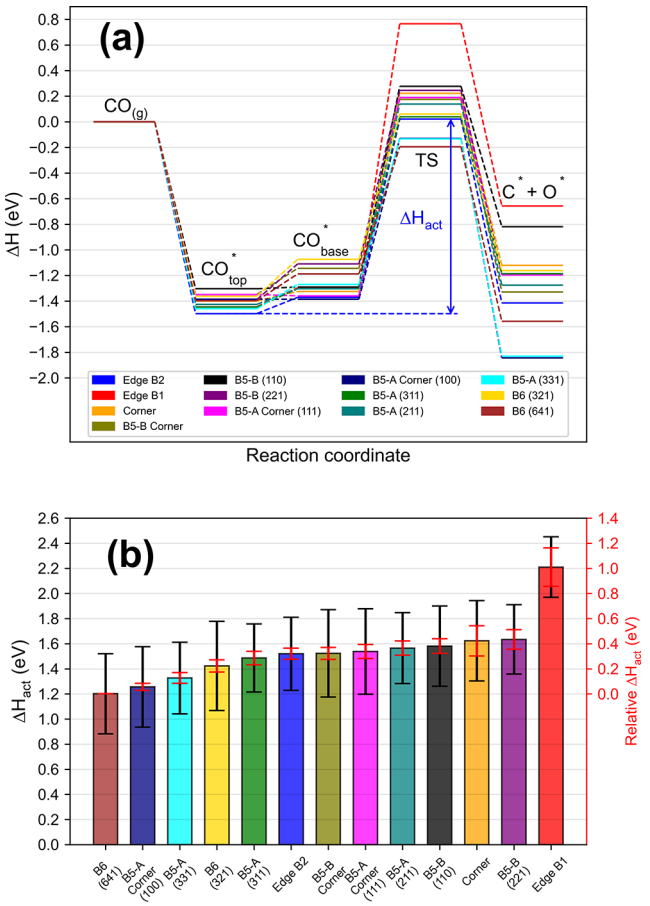

Figure 3. (a) Reaction enthalpy diagram (T = 0 K, ZPE included) for direct CO dissociation on the different types of low-coordinated sites identified in this study and (b) bar plot of the activation enthalpies (calculated as $\Delta H_{TS} - \Delta H_{top}$). The relative enthalpies in (b) are calculated based on the ΔH_{act} for the B6 (641) site. Error bars for both the absolute and relative activation enthalpies are the standard deviations obtained from the energies calculated with the 2000 GGA functionals of the BEEF-vdW ensemble.[58]

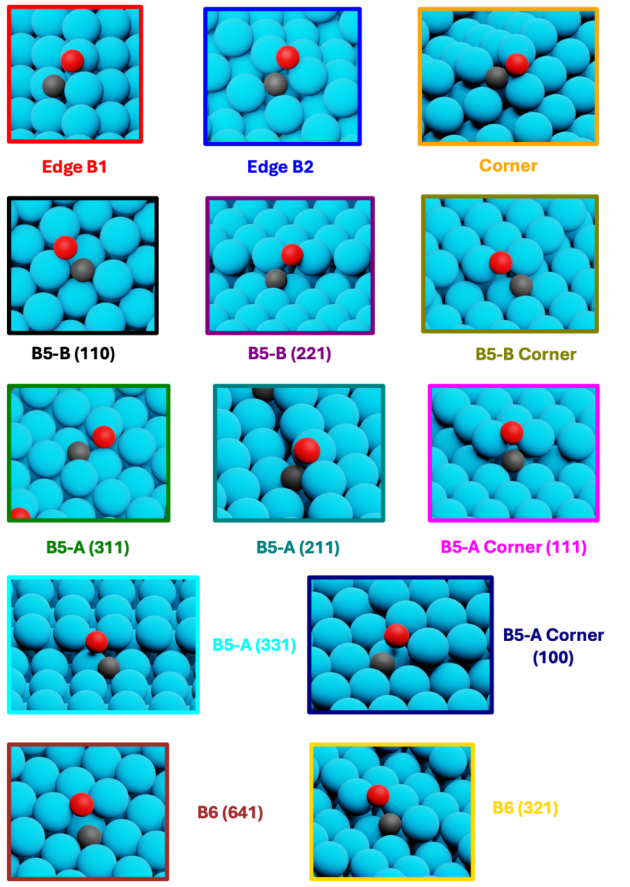

Figure 4. Snapshots of the calculated transition states on the 13 low-coordinate fcc sites identified in this work.

observations for the CO surface phases at low coverages both on Co terraces and steps.[70−73] Snapshots of the calculated transition states (TS) are shown in Figure 4, while the energetics of the full reaction paths are shown in Table S2. We can classify the different TSs in three groups depending on the location of the C atom: in the first, that applies only to the Edge B1 site, C is in a 3-fold site; in the second, that includes all the B5-B sites, the C atom is located in a nonplanar 4-fold site; and in the third, which occurs on the Edge B2, Corner, and all B5-A and B6 sites, the C atom inserts in a planar 4-fold site. The calculated activation enthalpies are compared in Figure 3b, with the uncertainty of the used DFT functional BEEF-vdW being indicated for the individual values but also relative to each other, thus giving a confidence measure of the observed trends.[74,75] Our calculations reveal that the different LCS can be characterized by drastically different reactivities, with the activation enthalpies spanning between 1.20 and 2.21 eV. We note that the only site where C is in a 3-fold position, namely the Edge B1, is by far the least reactive. The sites where C is in the nonplanar square site are mostly found on the low-reactivity end of the plot, and the most active LCS are those where C inserts in the planar 4-fold sites, underscoring the importance of this surface conformation for direct CO dissociation. We note that the low reactivity of the Edge B1 site has also been previously reported by Casey-Stevens et al. for N_2 dissociation in the case of Ru.[44] While several of the identified LCS are characterized by similar ΔH_{act} values ranging roughly between 1.5 and 1.6 eV, we can single out four most reactive sites that are the B6 (321), B5-A (331), B5-A Corner (100), and B6 (641) with E_{act} = 1.42, 1.33, 1.26, and 1.20 eV, respectively. Despite being by far the most active sites, we are not aware of previous theoretical studies that modeled the last three when investigating the mechanism of FT reaction on fcc-Co catalysts.[76] In particular, the most active sites here have at least a 0.2 eV lower CO splitting barrier than the most active fcc kink sites reported to date by Petersen, i.e., the B6 (321).[15]

It is worth mentioning that the focus of this study is a comparison of the various facets present on fcc-Co particles. Hence, we only discuss the direct pathway for CO dissociation as a simple test reaction but note that alternative H-assisted mechanisms have been previously proposed.[13,35,37,77] Nonetheless, these are predominant on the Co (111) and (0001) terraces, while CO dissociation has been shown to occur on the LCS,[38,78] where DFT calculations predict that the direct route is more facile.[15,16,62] Furthermore, recent CO scrambling experiments indicate a preference for direct CO dissociation on Co catalysts.[38,79]

As shown in Figure 2b, we predict the concentration of the most active sites to increase with particle size, which is in line with the widely reported structure sensitivity of Co NPs below 10−15 nm,[80−90] often linked to the increase of CO-splitting sites with D_{Co} in this size range, which is confirmed by our

https://doi.org/10.1021/acs.jpcc.5c07278
J. Phys. Chem. C 2025, 129, 21634−21641

calculations as well as by other theoretical studies.[32−34,91] Nonetheless, we note that these conclusions are valid for Co NPs in a vacuum, which might undergo significant surface reconstruction when exposed to FT conditions of high CO pressures.[80,81,92−95] In our recently published work, we have adapted our methodology to also account for the effect of CO, which was shown to alter the surface site percentages but not their nature.[96] Additionally, while here we focus on the fcc-Co lattice, real FT catalysts will have both hcp and fcc phases, limiting the extent to which the results of this study can be transferred to technical FT catalysts. We further note that our nanoparticle models rely on a fixed fcc lattice grid, thus assuming idealized structures that neglect possible strain-induced reconstructions or support effects at the metal−support interface.

These results offer an interesting new perspective on the success achieved by previous theoretical studies that chose the fcc (211) surface as representative of the LCS on catalyst NPs. Albeit this conformation constitutes a rather minor portion of all the LCS for all particle sizes as shown in Figure 2a (their highest concentration is ∼8% for the 10 nm particles), we observe from Figure 3b that 8 of the 13 identified LCS are characterized by a ΔH_{act} that is in the ±0.1 eV range from that of the B5-A (211) sites. This highlights that, despite its low concentration, the fcc (211) facet ends up capturing the reactivity of the majority of the active sites, explaining why, by modeling this surface, theoretical studies have often achieved good agreement with experiments. Interestingly, despite being completely absent on the small particles, the B5-A (211) would accidentally provide a good description of their reactivity, as it displays a ΔH_{act} close to those of the Edge B2 and Corner sites, which are the most abundant LCS for NPs < 6 nm. However, while the B5-A (211) sites display similar reactivity to that of the majority of the LCS, they are not among the most active sites on the fcc-Co particles. This underscores the necessity of a more thorough screening of the different LCS to ensure accurate theoretical modeling of chemical reactions.

Comparing our results to the literature (see Table S3), we note that they are typically within the standard deviations obtained from the BEEF-vdW ensemble,[58] which range between 0.24 and 0.36 eV. Importantly, the uncertainties are significantly reduced when the reactivities of the different LCS sites are compared among each other rather than considered as absolute values. This is shown by the error bars reported in red in Figure 3b, which are the standard deviations of the ΔH_{act} relative to the B6 (641) site, which are drastically smaller as most of them are below 0.05 eV, highlighting the accuracy of DFT when comparing trends.[97,98] This is confirmed by the data presented in Table S2, where we show that, despite the reaction barriers calculated in this study being significantly larger, they are all so by about 0.2−0.3 eV in respect to those reported by Petersen,[15] revealing the systematic shift that occurs when calculating the same barriers with different functionals.

In Figure 5, we show that the reactivity of the different sites is well described by the Brønsted−Evans−Polanyi (BEP) relation,[99−101] with the exception of the least active edge B2 site, where the TS lies significantly above the correlation line and hence is left out. Another, albeit smaller, outlier is the most active B6 (641) site, where the TS lies below the correlation line. The most stable FSs are those for the B5-A (331) and B5-A Corner (100) sites, likely because both C and O occupy 4-fold sites, which are the most favorable ones for both species. As shown in Figure S27, a similarly good correlation is obtained between the ΔH_{TS} and ΔH_{FS} when they are considered in respect to $CO_{(g)}$ rather than adsorbed on top position. Furthermore, we demonstrate that C adsorption is a rather accurate reactivity descriptor in Figures S28−S29, where we show that the correlations between ΔH_{TS} and C ΔH_{ads}, including all the data points, yield small MAEs of 0.085 and 0.059 eV when CO on the top position and $CO_{(g)}$ are considered as reference states, respectively. Interestingly, this indicates that undercoordinated sites follow a similar BEP relationship, although with a rather small slope of 0.42, but differ in TS and FS, whereas surfaces without undercoordinated sites (e.g., (111)) follow higher-lying BEP relations with a higher intercept.[102]

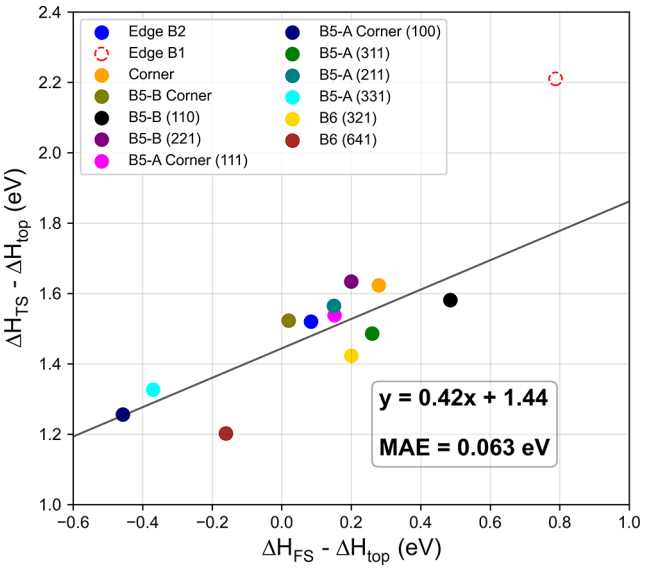

Figure 5. Brønsted−Evans−Polanyi (BEP) relation for direct CO dissociation on the low-coordinated sites investigated in this study. The data point relative to the edge B1 site was left out of the correlation. "MAE" stands for mean absolute error, where the error of each individual data point is the length of the normal segment connecting the point and the correlation line.

4. CONCLUSION

In summary, we have investigated a plethora of LCS of fcc-Co metal catalysts of different particle sizes by calculating direct CO dissociation barriers. We have shown that the activation enthalpies of the various LCS fall within a rather broad energy range and, to the best of our knowledge, the three most active sites have never been considered to model the FT reaction mechanism on Co, underscoring that classically neglected sites might play an important role in chemical reactions. Interestingly, all investigated LCS but one (i.e., the Edge B1 site) seems to obey the same BEP relationship. Furthermore, we investigated the most common sites for small particles in a comprehensive manner, showing that among them, only the Edge B2 site, which sits at the intersection of (111) and (100) terraces, displays reasonable barriers, being about 0.3 eV larger than those for the most active sites. Interestingly, the Edge B2 sites exhibit reaction barrier heights similar to those of the B5-A (211) sites, which are commonly used to model the steps of small nanoparticles despite being largely absent in practice, explaining their effectiveness in representing undercoordinated sites. However, we believe that the edge and corner sites are more realistic active site models when small NPs below 5 nm are simulated, and we

https://doi.org/10.1021/acs.jpcc.5c07278
J. Phys. Chem. C 2025, 129, 21634−21641

suggest that this also holds true for other transition metals as well as reactions.

■ ASSOCIATED CONTENT

Supporting Information

The Supporting Information is available free of charge at https://pubs.acs.org/doi/10.1021/acs.jpcc.5c07278.

Additional tables, figures, computational and methodological details for employed unit cells and *k*-point grids, site classification, CO adsorption energy calculations, full reaction paths for direct CO dissociation, comparison with previous studies, and further scaling relations (PDF)

Coordinates in *xyz* format and energies of all DFT-calculated structures (TXT)

■ AUTHOR INFORMATION

Corresponding Author

Felix Studt − *Institute of Catalysis Research and Technology, Karlsruhe Institute of Technology, Eggenstein-Leopoldshafen 76344, Germany; Institute for Chemical Technology and Polymer Chemistry, Karlsruhe Institute of Technology, Karlsruhe 76131, Germany;* orcid.org/0000-0001-6841-4232; Email: felix.studt@kit.edu

Authors

Enrico Sireci − *Institute of Catalysis Research and Technology, Karlsruhe Institute of Technology, Eggenstein-Leopoldshafen 76344, Germany*

Dmitry I. Sharapa − *Institute of Catalysis Research and Technology, Karlsruhe Institute of Technology, Eggenstein-Leopoldshafen 76344, Germany;* orcid.org/0000-0001-9510-9081

Complete contact information is available at: https://pubs.acs.org/10.1021/acs.jpcc.5c07278

Notes

The authors declare no competing financial interest.

■ ACKNOWLEDGMENTS

The authors gratefully acknowledge the financial support of the German Federal Ministry of Research, Technology and Space (BMFTR) within the CARE-OSENE project (03SF0673). The authors acknowledge support by the state of Baden-Württemberg through bwHPC and the German Research Foundation (DFG) through grant no. INST40/575-1FUGG (JUSTUS2cluster, RVs bw17D011). Support from the Helmholtz Association is also gratefully acknowledged.

■ REFERENCES

(1) Marakatti, V. S.; Gaigneaux, E. M. *Recent Advances in Heterogeneous Catalysis for Ammonia Synthesis*. *ChemCatChem* **2020**, *12*, 5838−5857.

(2) Humphreys, J.; Lan, R.; Tao, S. Development and Recent Progress on Ammonia Synthesis Catalysts for Haber−Bosch Process. *Adv. Energy Sustainability Res.* **2021**, *2*, 2000043.

(3) Schlögl, R. Catalytic Synthesis of Ammonia - A "Never-Ending Story"? *Angew. Chem., Int. Ed.* **2003**, *42*, 2004−2008.

(4) Martin, O.; Pérez-Ramírez, J. New and Revisited Insights into the Promotion of Methanol Synthesis Catalysts by CO2. *Catal. Sci. Technol.* **2013**, *3* (12), 3343−3352.

(5) van den Berg, R.; Prieto, G.; Korpershoek, G.; van der Wal, L. I.; van Bunningen, A. J.; Lægsgaard-Jørgensen, S.; de Jongh, P. E.; de Jong, K. P. Structure Sensitivity of Cu and CuZn Catalysts Relevant to Industrial Methanol Synthesis. *Nat. Commun.* **2016**, *7*, 13057.

(6) Behrens, M.; Studt, F.; Kasatkin, I.; Kühl, S.; Hävecker, M.; Abild-Pedersen, F.; Zander, S.; Girgsdies, F.; Kurr, P.; Kniep, B.-L.; et al. The Active Site of Methanol over Cu/ZnO/Al2O3 Industrial Catalysts. *Science* **2012**, *336* (6083), 893−897.

(7) De Smit, E.; Weckhuysen, B. M. The Renaissance of Iron-Based Fischer−Tropsch Synthesis: On the Multifaceted Catalyst Deactivation Behaviour. *Chem. Soc. Rev.* **2008**, *37* (12), 2758−2781.

(8) Khodakov, A. Y.; Chu, W.; Fongarland, P. Advances in the Development of Novel Cobalt Fischer−Tropsch Catalysts for Synthesis of Long-Chain Hydrocarbons and Clean Fuels. *Chem. Rev.* **2007**, *107*, 1692−1744.

(9) Carballo, J. M. G.; Yang, J.; Holmen, A.; García-Rodríguez, S.; Rojas, S.; Ojeda, M.; Fierro, J. L. G. Catalytic Effects of Ruthenium Particle Size on the Fischer−Tropsch Synthesis. *J. Catal.* **2011**, *284* (1), 102−108.

(10) Honkala, K.; Hellman, A.; Remediakis, I. N.; Logadottir, A.; Carlsson, A.; Dahl, S.; Christensen, C. H.; Nørskov, J. K. Ammonia Synthesis From-Principles Calculations. *Science* **2005**, *307* (5709), 555−558.

(11) Garden, A. L.; Skúlason, E. The Mechanism of Industrial Ammonia Synthesis Revisited: Calculations of the Role of the Associative Mechanism. *J. Phys. Chem. C* **2015**, *119* (47), 26554−26559.

(12) Ertl, G. Surface Science and Catalysis—Studies on the Mechanism of Ammonia Synthesis: The P. H. Emmett Award Address. *Catal. Rev.* **1980**, *21* (2), 201−223.

(13) Ojeda, M.; Nabar, R.; Nilekar, A. U.; Ishikawa, A.; Mavrikakis, M.; Iglesia, E. CO Activation Pathways and the Mechanism of Fischer−Tropsch Synthesis. *J. Catal.* **2010**, *272* (2), 287−297.

(14) Zhang, R.; Wang, Y.; Gaspard, P.; Kruse, N. The Oscillating Fischer−Tropsch Reaction. *Science* **2023**, *382* (6666), 99−103.

(15) Petersen, M. A.; Van Den Berg, J. -A.; Ciobîcă, I. M.; Van Helden, P. Revisiting CO Activation on Co Catalysts: Impact of Step and Kink Sites from DFT. *ACS Catal.* **2017**, *7* (3), 1984−1992.

(16) Zijlstra, B.; Broos, R. J. P.; Chen, W.; Bezemer, G. L.; Filot, I. A. W.; Hensen, E. J. M. The Vital Role of Step-Edge Sites for Both CO Activation and Chain Growth on Cobalt Fischer−Tropsch Catalysts Revealed through First-Principles-Based Microkinetic Modeling Including Lateral Interactions. *ACS Catal.* **2020**, *10* (16), 9376−9400.

(17) Grajciar, L.; Heard, C. J.; Bondarenko, A. A.; Polynski, M. V.; Meeprasert, J.; Pidko, E. A.; Nachtigall, P. Towards Operando Computational Modeling in Heterogeneous Catalysis. *Chem. Soc. Rev.* **2018**, *47*, 8307−8348.

(18) Chen, B. W. J.; Xu, L.; Mavrikakis, M. Computational Methods in Heterogeneous Catalysis. *Chem. Rev.* **2021**, *121*, 1007−1048.

(19) Chizallet, C. Achievements and Expectations in the Field of Computational Heterogeneous Catalysis in an Innovation Context. *Top. Catal.* **2022**, *65* (1−4), 69−81.

(20) Conrad, H.; Ertl, G.; Koch, J.; Latta, E. E. Adsorption of CO on Pd Single Crystal Surfaces. *Surf. Sci.* **1974**, *43* (2), 462−480.

(21) Stuckless, J. T.; Al-Sarraf, N.; Wartnaby, C.; King, D. A. Calorimetric Heats of Adsorption for CO on Nickel Single Crystal Surfaces. *J. Chem. Phys.* **1993**, *99* (3), 2202−2212.

(22) Morgan, A. E.; Somorjai, G. A. Low Energy Electron Diffraction Studies of Gas Adsorption on the Platinum (100) Single Crystal Surface. *Surf. Sci.* **1968**, *12* (3), 405−425.

(23) Bonzel, H. P. The Role of Surface Science Experiments in Understanding Heterogeneous Catalysis. *Surf. Sci.* **1977**, *68* (68), 236−258.

(24) Ajo, H. M.; Ihm, H.; Moilanen, D. E.; Campbell, C. T. Calorimeter for Adsorption Energies of Larger Molecules on Single Crystal Surfaces. *Rev. Sci. Instrum.* **2004**, *75* (11), 4471−4480.

(25) Stuckless, J. T.; Starr, D. E.; Bald, D. J.; Campbell, C. T. Metal Adsorption Calorimetry and Adhesion Energies on Clean Single-Crystal Surfaces. *J. Chem. Phys.* **1997**, *107* (14), 5547−5553.

(26) Christmann, K.; Schober, O.; Ertl, G.; Neumann, M. Adsorption of Hydrogen on Nickel Single Crystal Surfaces. *J. Chem. Phys.* **1974**, *60*, 4528−4540.

(27) Lytken, O.; Lew, W.; Campbell, C. T. Catalytic Reaction Energetics by Single Crystal Adsorption Calorimetry: Hydrocarbons on Pt(111). *Chem. Soc. Rev.* **2008**, *37* (10), 2172−2179.
(28) Carabineiro, S. A. C.; Nieuwenhuys, B. E. Adsorption of Small Molecules on Gold Single Crystal Surfaces. *Gold Bull.* **2009**, *42*, 288−301.
(29) Wellendorff, J.; Silbaugh, T. L.; Garcia-Pintos, D.; Nørskov, J. K.; Bligaard, T.; Studt, F.; Campbell, C. T. A Benchmark Database for Adsorption Bond Energies to Transition Metal Surfaces and Comparison to Selected DFT Functionals. *Surf. Sci.* **2015**, *640*, 36−44.
(30) Van Santen, R. A. Complementary Structure Sensitive and Insensitive Catalytic Relationships. *Acc. Chem. Res.* **2009**, *42* (1), 57−66.
(31) Van Hardeveld, R.; Van Montfoort, A. The Influence of Crystallite Size on the Adsorption of Molecular Nitrogen on Nickel, Palladium and Platinum. *Surf. Sci.* **1966**, *4*, 396−430.
(32) Van Etten, M. P. C.; Zijlstra, B.; Hensen, E. J. M.; Filot, I. A. W. Enumerating Active Sites on Metal Nanoparticles: Understanding the Size Dependence of Cobalt Particles for CO Dissociation. *ACS Catal.* **2021**, *11*, 8484−8492.
(33) Sireci, E.; Grüger, T. D.; Plessow, P. N.; Sharapa, D. I.; Studt, F. Modeling the Shape and Stability of Co Nanoparticles as a Function of Size and Support Interactions through DFT Calculations and Monte Carlo Simulations. *J. Phys. Chem. C* **2025**, *129*, 13232−13243.
(34) van Helden, P.; Ciobîcă, I. M.; Coetzer, R. L. J. The Size-Dependent Site Composition of FCC Cobalt Nanocrystals. *Catal. Today* **2016**, *261*, 48−59.
(35) Van Helden, P.; Van Den Berg, J. A.; Ciobîcă, I. M. Hydrogen-Assisted CO Dissociation on the Co(211) Stepped Surface. *Catal. Sci. Technol.* **2012**, *2* (3), 491−494.
(36) Banerjee, A.; Van Bavel, A. P.; Kuipers, H. P. C. E.; Saeys, M. CO Activation on Realistic Cobalt Surfaces: Kinetic Role of Hydrogen. *ACS Catal.* **2017**, *7* (8), 5289−5293.
(37) Liu, J. X.; Su, H. Y.; Sun, D. P.; Zhang, B.-Y.; Li, W.-X. Crystallographic Dependence of CO Activation on Cobalt Catalysts: HCP versus FCC. *J. Am. Chem. Soc.* **2013**, *135* (44), 16284−16287.
(38) Chen, W.; Zijlstra, B.; Filot, I. A. W.; Pestman, R.; Hensen, E. J. M. Mechanism of Carbon Monoxide Dissociation on a Cobalt Fischer−Tropsch Catalyst. *ChemCatchem* **2018**, *10* (1), 136−140.
(39) Pestman, R.; Chen, W.; Hensen, E. Insight into the Rate-Determining Step and Active Sites in the Fischer−Tropsch Reaction over Cobalt Catalysts. *ACS Catal.* **2019**, *9* (5), 4189−4195.
(40) Swart, J. C. W. *A Theoretical View On Deactivation Of Cobalt-Based Fischer−Tropsch Catalysts*; Doctoral Thesis, University of Cape Town; 2008.
(41) Van Steen, E.; Claeys, M.; Dry, M. E.; Van De Loosdrecht, J.; Viljoen, E. L.; Visagie, J. L. Stability of Nanocrystals: Thermodynamic Analysis of Oxidation and Re-Reduction of Cobalt in Water/Hydrogen Mixtures. *J. Phys. Chem. B* **2005**, *109* (8), 3575−3577.
(42) Rahmati, M.; Safdari, M. S.; Fletcher, T. H.; Argyle, M. D.; Bartholomew, C. H. Chemical and Thermal Sintering of Supported Metals with Emphasis on Cobalt Catalysts during Fischer−Tropsch Synthesis. *Chem. Rev.* **2020**, *120* (10), 4455−4533.
(43) Dietze, E. M.; Plessow, P. N.; Studt, F. Modeling the Size Dependency of the Stability of Metal Nanoparticles. *J. Phys. Chem. C* **2019**, *123* (41), 25464−25469.
(44) Casey-Stevens, C. A.; Lambie, S. G.; Ruffman, C.; Skúlason, E.; Garden, A. L. Geometric and Electronic Effects Contributing to N2 Dissociation Barriers on a Range of Active Sites on Ru Nanoparticles. *J. Phys. Chem. C* **2019**, *123* (50), 30458−30466.
(45) Cheng, J.; Gong, X.-Q.; Hu, P.; Lok, C. M.; Ellis, P.; French, S. A Quantitative Determination of Reaction Mechanisms from Density Functional Theory Calculations: Fischer−Tropsch Synthesis on Flat and Stepped Cobalt Surfaces. *J. Catal.* **2008**, *254* (2), 285−295.
(46) Mohsenzadeh, A.; Richards, T.; Bolton, K. DFT Study of the Water Gas Shift Reaction on Ni(111), Ni(100) and Ni(110) Surfaces. *Surf. Sci.* **2016**, *644*, 53−63.
(47) Filot, I. A. W.; Van Santen, R. A.; Hensen, E. J. M. The Optimally Performing Fischer−Tropsch Catalyst. *Angew. Chem., Int. Ed.* **2014**, *53* (47), 12746−12750.
(48) Van Helden, P.; Berg, J. A. V. D.; Petersen, M. A.; Janse Van Rensburg, W.; Ciobîcă, I. M.; Van De Loosdrecht, J. Computational Investigation of the Kinetics and Mechanism of the Initial Steps of the Fischer−Tropsch Synthesis on Cobalt. *Faraday Discuss.* **2017**, *197*, 117−151.
(49) Fajín, J. L. C.; Cordeiro, M. N. D. S.; Gomes, J. R. B. DFT Study on the Reaction of NO Oxidation on a Stepped Gold Surface. *Appl. Catal., A* **2010**, *379* (1−2), 111−120.
(50) Liu, Z. P.; Hu, P. General Rules for Predicting Where a Catalytic Reaction Should Occur on Metal Surfaces: A Density Functional Theory Study of C-H and C-O Bond Breaking/Making on Flat, Stepped, and Kinked Metal Surfaces. *J. Am. Chem. Soc.* **2003**, *125* (7), 1958−1967.
(51) Mallikarjun Sharada, S.; Bligaard, T.; Luntz, A. C.; Kroes, G. J.; Nørskov, J. K. SBH10: A Benchmark Database of Barrier Heights on Transition Metal Surfaces. *J. Phys. Chem. C* **2017**, *121* (36), 19807−19815.
(52) Fajín, J. L. C.; Cordeiro, M. N. D. S.; Illas, F.; Gomes, J. R. B. Influence of Step Sites in the Molecular Mechanism of the Water Gas Shift Reaction Catalyzed by Copper. *J. Catal.* **2009**, *268* (1), 131−141.
(53) Migliorini, D.; Chadwick, H.; Nattino, F.; Gutiérrez-González, A.; Dombrowski, E.; High, E. A.; Guo, H.; Utz, A. L.; Jackson, B.; Beck, R. D.; Kroes, G.-J. Surface Reaction Barriometry: Methane Dissociation on Flat and Stepped Transition-Metal Surfaces. *J. Phys. Chem. Lett.* **2017**, *8* (17), 4177−4182.
(54) Yang, M.-L.; Zhu, Y.-A.; Fan, C.; Sui, Z.-J.; Chen, D.; Zhou, X. G. DFT Study of Propane Dehydrogenation on Pt Catalyst: Effects of Step Sites. *Phys. Chem. Chem. Phys.* **2011**, *13* (8), 3257−3267.
(55) Petersen, M. A.; Van Den Berg, J.-A.; Ciobîcă, I. M.; Van Helden, P. Revisiting CO Activation on Co Catalysts: Impact of Step and Kink Sites from DFT. *ACS Catal.* **2017**, *7* (3), 1984−1992.
(56) Kresse, G.; Furthmüller, J. Efficiency of Ab-Initio Total Energy Calculations for Metals and Semiconductors Using a Plane-Wave Basis Set. *Comput. Mater. Sci.* **1996**, *6*, 15−50.
(57) Kresse, G.; Hafner, J. Ab Initio Molecular Dynamics for Liquid Metals. *Phys. Rev. B* **1993**, *47* (1), 558.
(58) Wellendorff, J.; Lundgaard, K. T.; Møgelhøj, A.; Petzold, V.; Landis, D. D.; Nørskov, J. K.; Bligaard, T.; Jacobsen, K. W. Density Functionals for Surface Science: Exchange-Correlation Model Development with Bayesian Error Estimation. *Phys. Rev. B:Condens. Matter Mater. Phys.* **2012**, *85* (23), 235149.
(59) Kresse, G.; Joubert, D. From Ultrasoft Pseudopotentials to the Projector Augmented-Wave Method. *Phys. Rev. B* **1999**, *59* (3), 1758−1775.
(60) Henkelman, G.; Jónsson, H. A Dimer Method for Finding Saddle Points on High Dimensional Potential Surfaces Using Only First Derivatives. *J. Chem. Phys.* **1999**, *111* (15), 7010−7022.
(61) Gunasooriya, G. T. K. K.; Van Bavel, A. P.; Kuipers, H. P. C. E.; Saeys, M. CO Adsorption on Cobalt: Prediction of Stable Surface Phases. *Surf. Sci.* **2015**, *642*, L6−L10.
(62) Zijlstra, B.; Broos, R. J. P.; Chen, W.; Oosterbeek, H.; Filot, I. A. W.; Hensen, E. J. M. Coverage Effects in CO Dissociation on Metallic Cobalt Nanoparticles. *ACS Catal.* **2019**, *9* (8), 7365−7372.
(63) van Hardeveld, R.; Hartog, F. The Statistics of Surface Atoms and Surface Sites on Metal Crystals. *Surf. Sci.* **1969**, *15*, 189−230.
(64) Zhou, M.; Liu, B. First-Principles Investigation of Adsorbate-Adsorbate Interactions on Ni(111), Ni(211), and Ni(100) Surfaces. *Ind. Eng. Chem. Res.* **2017**, *56* (20), 5813−5820.
(65) Zhi, C.; Zhang, R.; Wang, B. Comparative Studies about CO Methanation over Ni(211) and Zr-Modified Ni(211) Surfaces: Qualitative Insight into the Effect of Surface Structure and Composition. *Mol. Catal.* **2017**, *438*, 1−14.
(66) Shi, H.; Xia, M.; Lu, H.; Xie, Q.; Jia, L.; Hou, B.; Xiao, Y.; Li, D. Theoretical Investigation of the Reactivity of Flat Ni (111) and Stepped Ni (211) Surfaces for Acetic Acid Hydrogenation to Ethanol. *Int. J. Hydrogen Energy* **2021**, *46* (29), 15454−15470.

https://doi.org/10.1021/acs.jpcc.5c07278
J. Phys. Chem. C 2025, 129, 21634−21641

(67) Tuo, Y.; Yang, L.; Cheng, H.; Yang, M.; Zhu, Y. A.; Li, P. Density Functional Theory Study of Decalin Dehydrogenation for Hydrogen Release on Pt(111) and Pt(211). *Int. J. Hydrogen Energy* **2018**, *43* (42), 19575−19588.
(68) Catapan, R. C.; Oliveira, A. A. M.; Chen, Y.; Vlachos, D. G. DFT Study of the Water-Gas Shift Reaction and Coke Formation on Ni(111) and Ni(211) Surfaces. *J. Phys. Chem. C* **2012**, *116* (38), 20281−20291.
(69) Daigle, A. D.; Belbruno, J. J. Density Functional Theory Study of the Adsorption of Oxygen Atoms on Gold (111), (100) and (211) Surfaces. *Surf. Sci.* **2011**, *605* (13−14), 1313−1319.
(70) Papp, H. Chemisorption and Reactivity of Carbon Monoxide on a Co(11−20) Single Crystal Surface: Studied by LEED, UPS, EELS, AES and Work Function Measurements. *Surf. Sci.* **1985**, *149*, 460−470.
(71) Papp, H. The Chemisorption of Carbon Monoxide on a Co(0001) Single Crystal Surface; Studied by LEED, UPS, EELS, AES and Work Function Measurements. *Surf. Sci.* **1983**, *129*, 205−218.
(72) Papp, H. The Chemisorption of Carbon Monoxide on a Co(1O-1O) Single Crystal Surface. Studied by LEED, UPS, EELS, AES and Work Function Measurements. *Ber. Bunseges. Phys. Chem.* **1982**, *86*, 555−562.
(73) Toomes, R. L.; King, D. A. The Adsorption of CO on Co(1010). *Surf. Sci.* **1996**, *349*, 1−18.
(74) Medford, A. J.; Wllendorff, J.; Vojvodic, A.; Studt, F.; Abild-Pedersen, F.; Jacobsen, K. W.; Bligaard, T.; Nørskov, J. K. Assessing the Reliability of Calculated Catalytic Ammonia Synthesis Rates. *Science* **2014**, *345* (6193), 197−200.
(75) Garcia-Pintos, D.; Voss, J.; Jensen, A. D.; Studt, F. Hydrodeoxygenation of Phenol to Benzene and Cyclohexane on Rh(111) and Rh(211) Surfaces: Insights from Density Functional Theory. *J. Phys. Chem. C* **2016**, *120* (33), 18529−18537.
(76) Rommens, K. T.; Saeys, M. Molecular Views on Fischer−Tropsch Synthesis. *Chem. Rev.* **2023**, *123* (9), 5798−5858.
(77) Visconti, C. G.; Tronconi, E.; Lietti, L.; Forzatti, P.; Rossini, S.; Zennaro, R. Detailed Kinetics of the Fischer−Tropsch Synthesis on Cobalt Catalysts Based on H-Assisted CO Activation. *Top. Catal.* **2011**, *54* (13), 786.
(78) Böller, B.; Durner, K. M.; Wintterlin, J. The Active Sites of a Working Fischer−Tropsch Catalyst Revealed by Operando Scanning Tunnelling Microscopy. *Nat. Catal.* **2019**, *2* (11), 1027−1034.
(79) Chen, W.; Filot, I. A. W.; Pestman, R.; Hensen, E. J. M. Mechanism of Cobalt-Catalyzed CO Hydrogenation: 2. Fischer−Tropsch Synthesis. *ACS Catal.* **2017**, *7* (12), 8061−8071.
(80) Bezemer, G. L.; Bitter, J. H.; Kuipers, H. P. C. E.; Oosterbeek, H.; Holewijn, J. E.; Xu, X.; Kapteijn, F.; van Dillen, A. J.; De Jong, K. P. Cobalt Particle Size Effects in the Fischer−Tropsch Reaction Studied with Carbon Nanofiber Supported Catalysts. *J. Am. Chem. Soc.* **2006**, *128* (12), 3956−3964.
(81) Prieto, G.; Martínez, A.; Concepción, P.; Moreno-Tost, R. Cobalt Particle Size Effects in Fischer−Tropsch Synthesis: Structural and in Situ Spectroscopic Characterisation on Reverse Micelle-Synthesised Co/ITQ-2 Model Catalysts. *J. Catal.* **2009**, *266* (1), 129−144.
(82) Yang, J.; Tveten, E. Z.; Chen, D.; Holmen, A. Understanding the Effect of Cobalt Particle Size on Fischer−Tropsch Synthesis: Surface Species and Mechanistic Studies by SSITKA and Kinetic Isotope Effect. *Langmuir* **2010**, *26* (21), 16558−16567.
(83) Herranz, T.; Deng, X.; Cabot, A.; Guo, J.; Salmeron, M. Influence of the Cobalt Particle Size in the CO Hydrogenation Reaction Studied by in Situ X-Ray Absorption Spectroscopy. *J. Phys. Chem. B* **2009**, *113* (31), 10721−10727.
(84) Fischer, N.; Van Steen, E.; Claeys, M. Structure Sensitivity of the Fischer−Tropsch Activity and Selectivity on Alumina Supported Cobalt Catalysts. *J. Catal.* **2013**, *299*, 67−80.
(85) Eschemann, T. O.; Lamme, W. S.; Manchester, R. L.; Parmentier, T. E.; Cognigni, A.; Rønning, M.; De Jong, K. P. Effect of Support Surface Treatment on the Synthesis, Structure, and Performance of Co/CNT Fischer−Tropsch Catalysts. *J. Catal.* **2015**, *328*, 130−138.
(86) Melaet, G.; Lindeman, A. E.; Somorjai, G. A. Cobalt Particle Size Effects in the Fischer−Tropsch Synthesis and in the Hydrogenation of CO2 Studied with Nanoparticle Model Catalysts on Silica. *Top. Catal.* **2014**, *57* (6−9), 500−507.
(87) Ralston, W. T.; Melaet, G.; Saephan, T.; Somorjai, G. A. Evidence of Structure Sensitivity in the Fischer−Tropsch Reaction on Model Cobalt Nanoparticles by Time-Resolved Chemical Transient Kinetics. *Angew. Chem., Int. Ed.* **2017**, *129* (26), 7523−7527.
(88) Xiong, H.; Motchelaho, M. A. M.; Moyo, M.; Jewell, L. L.; Coville, N. J. Correlating the Preparation and Performance of Cobalt Catalysts Supported on Carbon Nanotubes and Carbon Spheres in the Fischer−Tropsch Synthesis. *J. Catal.* **2011**, *278* (1), 26−40.
(89) Van de Loosdrecht, J.; Botes, F. G.; Ciobîcă, I. M.; Ferreira, A. C.; Gibson, P.; Moodley, D. J.; Saib, A. M.; Visagie, J. L.; Weststrate, C. J.; Niemantsverdriet, J. W.Fischer−Tropsch Synthesis: Catalysts and Chemistry*Comprehensive Inorganic Chemistry II: From Elements to Applications*Elsevier20137525−557
(90) Tuxen, A.; Carenco, S.; Chintapalli, M.; Chuang, C. H.; Escudero, C.; Pach, E.; Jiang, P.; Borondics, F.; Beberwyck, B.; Alivisatos, A. P.; Thornton, G.; Pong, W. F.; Guo, J.; Perez, R.; Besenbacher, F.; Salmeron, M. Size-Dependent Dissociation of Carbon Monoxide on Cobalt Nanoparticles. *J. Am. Chem. Soc.* **2013**, *135* (6), 2273−2278.
(91) Spanò, G.; Ferri, M.; Cheula, R.; Monai, M.; Weckhuysen, B. M.; Maestri, M. Deciphering Size and Shape Effects on the Structure Sensitivity of the CO2Methanation Reaction on Nickel. *ACS Catal.* **2025**, *15*, 8194−8203.
(92) Wilson, J.; De Groot, C. Atomic-Scale Restructuring in High-Pressure Catalysis. *J. Phys. Chem.* **1995**, *99*, 7860−7866.
(93) Banerjee, A.; Van Bavel, A. P.; Kuipers, H. P. C. E.; Saeys, M. Origin of the Formation of Nanoislands on Cobalt Catalysts during Fischer−Tropsch Synthesis. *ACS Catal.* **2015**, *5* (8), 4756−4760.
(94) Banerjee, A.; Navarro, V.; Frenken, J. W. M.; van Bavel, A. P.; Kuipers, H. P. C. E.; Saeys, M. Shape and Size of Cobalt Nanoislands Formed Spontaneously on Cobalt Terraces during Fischer−Tropsch Synthesis. *J. Phys. Chem. Lett.* **2016**, *7* (11), 1996−2001.
(95) Navarro, V.; Van Spronsen, M. A.; Frenken, J. W. M. In Situ Observation of Self-Assembled Hydrocarbon Fischer−Tropsch Products on a Cobalt Catalyst. *Nat. Chem.* **2016**, *8* (10), 929−934.
(96) Sireci, E.; Grüger, T. D.; Plessow, P. N.; Sharapa, D. I.; Studt, F. Modeling the Shape and Stability of Supported Co Nanoparticles under Fischer−Tropsch Conditions via DFT Calculations and Monte Carlo Simulations: Insights into CO-Driven Surface Reconstruction. *Catal. Sci. Technol.* **2025**, *15*, 6703−6715.
(97) Amsler, J.; Sarma, B. B.; Agostini, G.; Prieto, G.; Plessow, P. N.; Studt, F. Prospects of Heterogeneous Hydroformylation with Supported Single Atom Catalysts. *J. Am. Chem. Soc.* **2020**, *142* (11), 5087−5096.
(98) Plessow, P. N.; Studt, F. How Accurately Do Approximate Density Functionals Predict Trends in Acidic Zeolite Catalysis? *J. Phys. Chem. Lett.* **2020**, *11* (11), 4305−4310.
(99) Michaelides, A.; Liu, Z. P.; Zhang, C. J.; Alavi, A.; King, D. A.; Hu, P. Identification of General Linear Relationships between Activation Energies and Enthalpy Changes for Dissociation Reactions at Surfaces. *J. Am. Chem. Soc.* **2003**, *125* (13), 3704−3705.
(100) Pallassana, V.; Neurock, M. Electronic Factors Governing Ethylene Hydrogenation and Dehydrogenation Activity of Pseudomorphic PdML/Re(0001), PdML/Ru(0001), Pd(111), and PdML/Au(111) Surfaces. *J. Catal.* **2000**, *191* (2), 301−317.
(101) Hammer, B.; Nørskov, J. K. Theoretical Surface Science and Catalysis—Calculations and Concepts. *Adv. Catal.* **2000**, *45* (C), 71−129.
(102) Nørskov, J. K.; Bligaard, T.; Logadottir, A.; Bahn, S.; Hansen, L. B.; Bollinger, M.; Bengaard, H.; Hammer, B.; Sljivancanin, Z.; Mavrikakis, M.; Xu, Y.; Dahl, S.; Jacobsen, C. J. H. Universality in Heterogeneous Catalysis. *J. Catal.* **2002**, *209* (2), 275−278.

https://doi.org/10.1021/acs.jpcc.5c07278
J. Phys. Chem. C 2025, 129, 21634−21641